RSC Advances

PAPER

View Article Online
View Journal | View Issue

Cite this: RSC Adv., 2014, 4, 32538

Microwave hydrothermal synthesis and gas sensing application of porous ZnO core–shell microstructures†

Xiaowei Li,[a] Xin Zhou,[a] Yang Liu,[a] Peng Sun,*[a] Kengo Shimanoe,[b] Noboru Yamazoe[b] and Geyu Lu*[a]

Received 25th April 2014
Accepted 18th July 2014

DOI: 10.1039/c4ra03789h

www.rsc.org/advances

A ZnO core–shell structure with a movable core inside a hollow shell has been rapidly prepared by an efficient microwave hydrothermal method without any template. The synthesis was performed in an aqueous solution using zinc acetate dihydrate as the precursor. The observations of field emission electron microscopy and transmission electron microscopy showed that these ZnO core–shell structures were composed of numerous primary particles with size of tens of nanometers. A series of time-dependent experiments were carried out in order to have a closer inspection of the evolution processes of such structures. When evaluated as a sensing material for gas sensors, the as-synthesized ZnO core–shell structures displayed a high response towards ethanol and good response-recovery properties.

1 Introduction

As an attractive wide-band-gap semiconductor (E_g = 3.37 eV at 300 K), zinc oxide (ZnO) has been extensively investigated mainly owing to its myriad technologically important applications including field effect transistors,[1,2] solar cells,[3] photocatalysts,[4] luminescent materials,[5,6] chemical sensors,[7] and so on. Since the properties of semiconducting materials are closely related to their morphology, grain size, crystallization, and specific area,[8–11] tremendous efforts have been dedicated to the rational design of novel and complex architectures. In order to highlight some special properties demanded by particular technological applications, various nanostructures have been synthesized, such as porous nanoflakes,[12] straw bundle,[13] tower,[14] hollow spheres,[15–19] and three-dimensional hierarchical structure.[20–22]

Over the past few years, the developments in nanotechnology as well as synthetic methods have facilitated the precise morphology control of nano/micro architecture. The rattle-type structure represents a new class of special structures with a distinctive core@void@shell configuration. Such structures have attracted tremendous attention of scientists all over the world for their appealing architectures and tunable physical and chemical properties. Therefore, the rattle-type structures gradually develop into a potential research area in the advanced materials.[23] Owing to the unique architecture, consisting of a movable core, an interstitial hollow space and a diverse functionalities of shell, the rattle-type structures are endowed with remarkable advantages such as high surface area, low density, thus rendering them attractive for applications in drug delivery vehicles,[24] nanoreactors,[25] lithium-ion batteries,[26] gas sensor,[27] and catalysis.[28] Currently, most research activity are focusing on the preparation of core–shell structures with different components using various synthetic approaches.[29–31] One usual strategy is based on template-assisted process. The core particles are first coated with templates as sacrificial layers, followed by depositing another functional materials as spherical shell, then the sacrificial layers are selectively removed by using a etchant or treating with calcinations, leaving a cavity in the centre. Despite its conceptual simplicity, this approach generally exists many difficulties in practice, such as incompatibility between materials and templates, sophisticated synthetic procedures and safe removal of the templates.[32] For this reason, the design and synthesis of core–shell structures still have importantly scientific and practical significance. Recently, an alternative approach based on Kirkendall effect or Ostwald ripening is employed to synthesize the core–shell structures.[33,34] Although much progress has been made, most of these procedures are still inefficient and tedious. Thus, a simple and economical route without template for the preparation of core–shell structures still remains highly desired.

In this work, we present a facile and rapid microwave hydrothermal method for the synthesis of porous ZnO core–

[a]State Key Laboratory on Integrated Optoelectronics, College of Electronic Science and Engineering, Jilin University, Changchun, 130012, People's Republic of China. E-mail: spmaster2008@163.com; lugy@jlu.edu.cn; Fax: +86 431 85167808; Tel: +86 431 8516780

[b]Department of Energy and Material Sciences Faculty of Engineering Sciences, Kyushu University, Kasuga-shi, Fukuoka 816-8580, Japan

† Electronic supplementary information (ESI) available. See DOI: 10.1039/c4ra03789h

shell structures. In comparison with traditional heating methods, microwave irradiation can offer homogeneous internal heating, namely increasing the temperature of the entire reaction vessel simultaneously and rapidly.[35,36] In particular, the precise control of the reaction parameters can make it possible to successfully prepare high-quality inorganic semiconducting nanostructures.[32] Our synthesis was performed at 140 °C in a short time (within 90 min). It was found that the size and morphology of ZnO microspheres could be tailored by simply changing the ageing time. As demonstrated by experimental results, the morphology evolution was supposed to be coincident with classical Ostwald ripening process. In addition, the excellent gas sensing performances of the sensor based on this ZnO core–shell structures were investigated.

2 Experimental procedure

2.1 Synthesis and characterization of ZnO microstructure

All chemicals in this study were of analytical grade and directly used without further purification. ZnO core–shell structures were synthesized by a fast microwave hydrothermal route. Briefly, a 40 mL aqueous solution containing 0.22 g of zinc acetate dihydrate ($Zn(CH_3COO)_2 \cdot 2H_2O$), 0.12 g of trisodium citrate dihydrate ($Na_3C_6H_5O_7 \cdot 2H_2O$) and 0.06 g of urea ($CO(NH_2)_2$) was first prepared at room temperature. Then the solution was stirred for 10 min to get a homogeneous transparent mixture. Subsequently, the resulting mixture was transferred into 100 mL Teflon-lined autoclave and treated with a predetermined heating programme (first heated to 140 °C at a heating rate of 4 °C min^{-1} from room temperature, then maintained at 140 °C for 20 min, and then cooled down naturally) in a microwave hydrothermal system. The precipitate was collected and washed by centrifugation several times before drying at 80 °C for 12 h. Finally, the obtained powder was calcined at 500 °C for 2 h in muffle furnace.

X-ray diffraction (XRD) analysis was performed on a Rigaku D/max-2550 X-ray diffractometer with Cu Kα radiation (λ = 1.5406 Å) operating at 40 kV in the range of 20–80° (2θ). Field emission scanning electron microscopy (FESEM) images were taken on a JEOL JSM-7500F microscope operating at 15 kV. Transmission electron microscopic (TEM) and high resolution transmission electron microscopic (HRTEM) images were recorded on a JEOL JEM-2100F microscopy with an accelerating voltage of 200 kV. Nitrogen adsorption–desorption isotherm was measured on a Gemini VII surface area and porosity system at 77 K. Pore diameter distribution was calculated by Barrett–Joyner–Halenda (BJH) method using the adsorption branch of the isotherms.

2.2 Fabrication and measurement of gas sensors

To demonstrate the application in gas-sensing, gas sensors based on the as-obtained ZnO samples were fabricated as follows: the white ZnO powder was dispersed in the deionized water to form a homogeneous paste as sensing materials, which was subsequently coated onto a ceramic tube (4 mm in length, 1.2 mm in external diameter, and 0.8 mm in internal diameter, attached with a pair of gold electrodes) by a small brush to form a thick sensing film. A Ni–Cr alloy coil was inserted through the ceramic tube as a heater to control the operating temperature of the sensors. The structure of the sensor is schematically shown in Fig. S1.† The measurements of sensing properties were conducted on a static system under laboratory conditions (50 RH%, 25 °C). The detailed testing procedure was like this: the sensor was alternately placed into test chambers with pure air or target gas. The response of the sensor was defined as the ratio of the resistances of the sensor in air (R_a) to that in tested gases (R_g). The time taken by the sensor to achieve 90% of the total resistance change in the case of adsorption and desorption was defined as the response time and recovery time, respectively.

3 Results and discussion

3.1 Structural and morphological characteristics

Fig. 1a shows the typical X-ray diffraction (XRD) pattern of as-prepared powder. All of the diffraction peaks were coincident with those from the standard card no. 36-1451, that is, could be indexed as hexagonal wurtzite ZnO with lattice constants of a = 3.249 Å and c = 5.206 Å. Besides, no peaks from other impurities were detected, which indicated that the product was composed of pure ZnO crystals. The overall morphology of as-prepared ZnO sample is shown in Fig. 1b. It can be seen that the ZnO powder was composed of a number of uniform microspheres with diameters around 2 μm. The enlarged FESEM images as shown in Fig. 1c and d display the internal and external details of these ZnO microspheres. It is clearly observed the external spherical shell was consisted of plenty of nanoparticles and presented a rough and porous surface. The broken ZnO microstructure shown in Fig. 1d confirms that the thickness of spherical shell was about 200 nm, and a smaller ZnO sphere (~1 μm) was enclosed in the above spherical shell, which formed a potential core–shell structure.

Fig. 2a shows a typical TEM image of ZnO core–shell structure, from which the core@void@shell configuration got

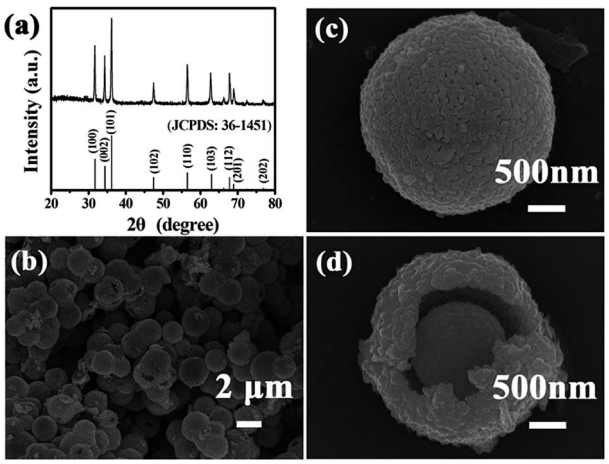

Fig. 1 (a) XRD pattern of the as-prepared product. (b) Typical FESEM image of ZnO microspheres. (c and d) High-magnification FESEM images of ZnO core–shell structure.

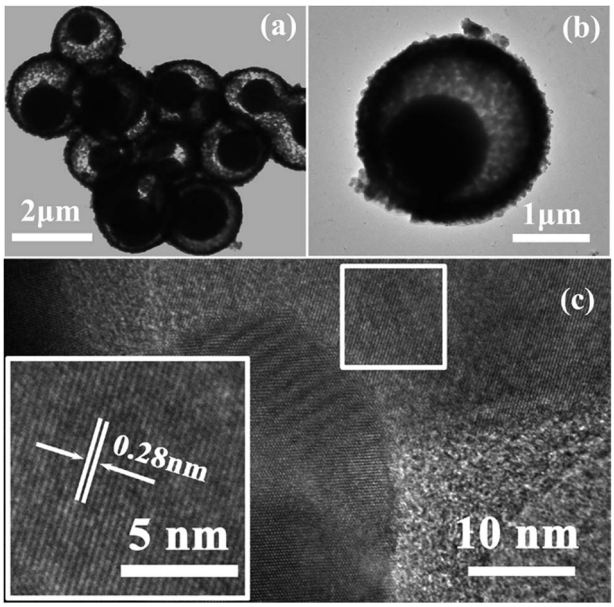

Fig. 2 (a) Low-magnification and (b) high-magnification transmission electron microscopy (TEM) image of the core–shell structure. (c) HRTEM images of the particles packed on the shell.

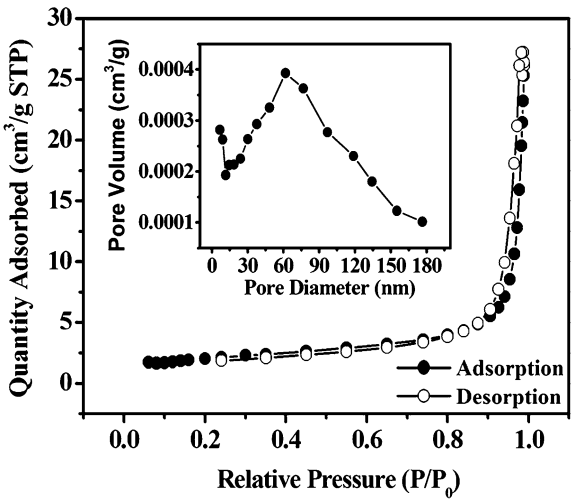

Fig. 3 Typical nitrogen adsorption–desorption isotherm and pore size distribution curve (inset) of ZnO yolk–shell microstructures.

further confirmed. The high-magnification TEM image of an individual ZnO microsphere in Fig. 2b reveals that the core–shell structure was in good accordance with the observation from the FESEM (Fig. 1d). Besides, based on the relative light contrast, the darker region in the center of the image indicated the solid interior of the movable ZnO core. To further examine the crystalline nature of the structures, the HRTEM image taken from the fringe of ZnO spherical shell is recorded in Fig. 2c. The result shows that each nanoparticle on the surface was highly crystalline with a lattice spacing of 0.28 nm, which was consistent with the distance between the {100} planes in the wurtzite ZnO.[37,38]

The N_2 adsorption–desorption isotherm and corresponding pore size distribution of the ZnO core–shell microstructures is displayed in Fig. 3. As can be seen, the adsorption–desorption isotherm exhibited stepwise adsorption and desorption with a hysteresis loop (type-III isotherm), suggesting the existence of disordered macropores in their structure. Pore size distribution curve (inset of Fig. 3) was calculated from the adsorption branch of nitrogen isotherm by the BJH method using the Halsey equation. It can be seen that the pore size was mainly distributed around the average size of 60 nm.

To get a better understanding on the evolution processes of these core–shell structure, the samples obtained at different time (see Fig. S2†) had been investigated and characterized by scanning electron microscopy (SEM) and transmission electron microscopy (TEM). The corresponding images are shown in Fig. 4a–d and S3.† The microstructure of the sample, which was collected at the moment when the synthetic processes steps into ageing stage, is shown in Fig. 4a. It can be seen that a spherical-shaped ZnO with smooth surface had been formed, and the diameter of the ZnO microspheres was about 1.5 μm. When the ageing time increased to 10 min, a typical core–shell structure showed up, accompanying a little increase of external diameter. Meanwhile, the nanoparticles aggregated on the surface of the spherical shell became larger (Fig. 4b). As the ageing time was prolonged to 20 min, these nanoparticles as well as the entire ZnO spherical shell continued to increase in size, while the internal ZnO core began to shrink gradually, which could be seen from Fig. 4c. For the sample having aged for half hour, as shown in Fig. 4d, the rattle-type structure evolved into traditional hollow structure due to the excessive ripening. On the basis of the foregoing results, the possible evolving process of these core–shell ZnO microstructures are illustrated schematically in Fig. 4e. The pristine ZnO solid microspheres were initially formed through hydrolysis and aggregation of tiny

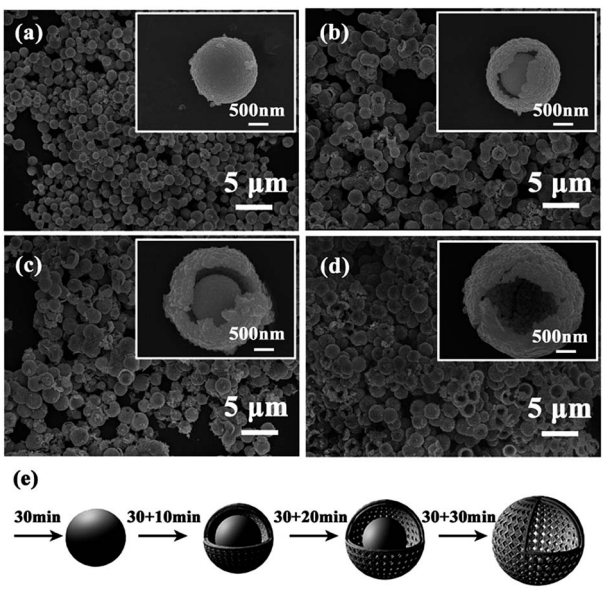

Fig. 4 (a–d) SEM images of the products obtained at different reaction stage after heat treatment. (e) Schematic illustration of the evolution process of spherical architectures.

nanocrystallites in ambient solution. With the extension of reaction time, the particles located underneath the surface layer began to dissolve, leading to an interstitial hollow space that divided the solid sphere into a movable core and an independent shell. Accompanied with the consumption of inner cores, the outward mass transfer processes from the cores along with recrystallization on the outer shells would happen instantaneously. As a result, the outer shells became larger but the cores smaller. With a further increase of the irradiating duration, the core was eventually disappeared, forming single-shell hollow microspheres at last. Therefore, it is believed that Ostwald ripening plays a vital role in the evolution process.[39–41]

3.2 Gas sensing properties

Recently, gas sensor, as an indispensable component in intelligent systems, has received considerable attention because of their potential applications in monitoring harmful gases threating domestic/public safety. Therefore, using the as-prepared ZnO core–shell structures and ZnO hollow microspheres as sensing materials, two gas sensors were fabricated and their gas sensing performances were investigated. Fig. 5a shows the response of the gas sensors to 200 ppm ethanol *versus* different operating temperatures ranging from 200 to 375 °C. It is obvious that the response of both tested sensors varied with operating temperature and exhibited a volcano-shaped curves. The response to ethanol first increased with the operating temperature, subsequently reached a maximum value at the operating temperature of 300 °C, and then gradually decreased with further increasing the operating temperature. Therefore, all of the subsequent sensing tests were proceeded at the optimal operating temperature of 300 °C. For ZnO core–shell structures, the maximum response value is 31, which is about 2 times higher than that of ZnO hollow microspheres. Further gas-sensing properties of the sensors to different concentrations of ethanol were investigated when the sensor working at optimal operation temperatures. As shown in Fig. 5b and its inset, the two curves of response exhibited approximately linear increase from 10 to 300 ppm, and then tended to saturation gradually after climbing over the point of 300 ppm. In particular, the discrepancy in response values and slope of the curve indicate that the sensing performance are highly dependent upon the microstructure of the ZnO powder.

The bar chart shown in Fig. 6a displays the response of the sensors when exposed to various volatile organic compounds (VOCs) gases, such as ethanol, formaldehyde, methanol, *etc.* All of these VOCs with same concentration of 200 ppm were tested at a working temperature of 300 °C. As expected, the sensor using the core–shell structures exhibited enhanced responses for each gas in comparison to hollow microspheres. It can be also observed that the sensor based on ZnO core–shell microstructures showed obvious response to ethanol, but little responses to other VOCs, which indicated that ZnO core–shell structures had an excellent selectivity towards ethanol as oppose to other gases.

It is well known that the response time and recovery time are also important parameters for evaluating a gas sensor. Rapid

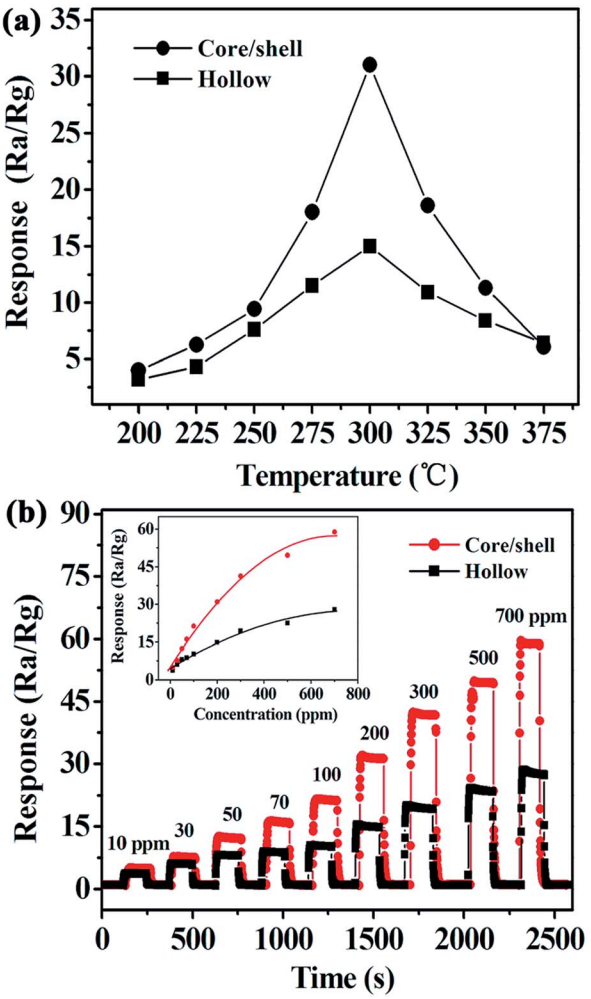

Fig. 5 (a) Responses of the sensors *versus* operating temperature to 200 ppm ethanol. (b) Responses of the sensors as a function of ethanol concentrations ranging from 10 to 700 ppm at optimal operation temperatures.

response and recovery are necessary in practical application. Fig. 6b presents the response transients of the sensor to 200 ppm ethanol at 300 °C. It can be seen that the resistance of the sensor changed immediately when ethanol was injected and then reached a steady state slowly. The time taken in this process was only 1 s. Soon afterwards, the sensor was transferred into air to recover and the time consumed by recovery was about 27 s. Moreover, the six periods of repetitive test shown in the inset of Fig. 6b indicated the good repeatability and stability of the sensor.

For the gas sensing mechanism of ZnO microstructures, the most acceptable model is based on the change in resistance, which is caused by the chemical adsorption and reaction of test gas molecules on the surface of the sensing materials.[42–44] Combining such classical theory with our practical results, the underlying sensing mechanism can be elucidated as follows: when the sensors fabricated by ZnO microstructures were exposed to air, oxygen molecules could easily adsorb to the exposed surfaces of these structures and capture free electron

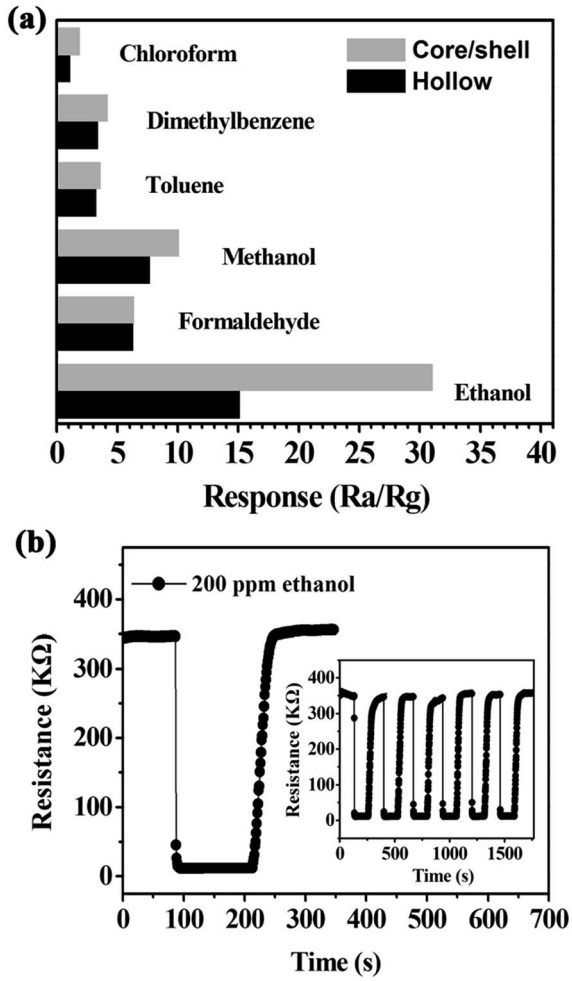

Fig. 6 (a) Comparison of responses to various VOCs at an operating temperature of 300 °C. (b) Dynamic curves of the sensor based on ZnO core–shell architectures to 200 ppm ethanol at 300 °C.

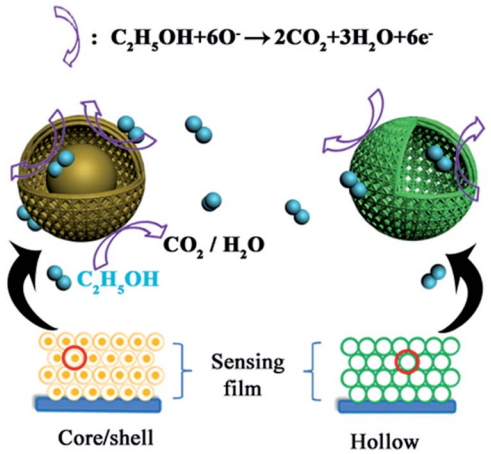

Fig. 7 Schematic diagrams of mass transportation and gas sensing principle.

from the conduction band of ZnO, existing as chemisorbed oxygen species (O^-, O_2^-, O^{2-}).[45–47] As a result, the electron concentration of sensing materials decreased, electron depletion layers would emerge on the surface of sensing materials, leading to the increase of the resistance. When the sensors were transferred to the vessel full of ethanol gas, adsorbed oxygen species on the surface would react with the reductive gas, the trapped electrons would be released back to the conduction band, which resulted in a decrease of the resistance.

The improvement of the sensing performance of the present ZnO core–shell structures are mainly ascribed to their unique configuration. Since the unique porous core–shell architecture possesses large numbers of well-defined pores on the surface domains, these pores in the structure could facilitate the diffusion and adsorption of the gas molecules. Moreover, compared with hollow spheres, the core–shell structures possess more exposed surface, which can provide plenty of active sites and space for redox reaction between ethanol gases and adsorbed oxygen, as shown in Fig. 7. That is, the utilization rate of the sensitive body is increased. Therefore, an enhanced gas response could be achieved using as-obtained ZnO core–shell architecture.

4 Conclusions

In conclusion, the core–shell ZnO was successfully synthesized by a simple microwave hydrothermal method without using any template. With the assistance of microwave irradiation, this preparation process could be limited to 90 minutes. As demonstrated by experimental results, microwave irradiation time played an important role in the formation of the ZnO core–shell structure. Further investigation on the evolution of ZnO microstructures reveals that the formation of the ZnO core–shell structure could be attributed to the Ostwald ripening process. In addition, the obtained product was utilized as sensing material for gas sensors and their sensing properties were investigated. The results indicated that the sensor based on ZnO core–shell structure exhibited high response and fast response and recover properties when detecting ethanol gases.

Acknowledgements

Thanks for the financial support from the National Nature Science Foundation of China (nos 61074172, 61134010, 61304242, 61374218 and 61327804) and Program for Chang Jiang Scholars and Innovative Research Team in University (no. IRT13018). National High-Tech Research and Development Program of China (863 Program, no. 2013AA030902).

Notes and references

1 S. Ju, K. Lee, D. B. Janes, M. H. Yoon, A. Facchetti and T. J. Marks, *Nano Lett.*, 2005, **5**, 2281.
2 W. K. Hong, J. I. Sohn, D. K. Hwang, S. S. Kwon, G. Jo, S. Song, S. M. Kim, H. J. Ko, S. J. Park and M. E. Welland, *Nano Lett.*, 2008, **8**, 950.
3 E. Galoppini, J. Rochford, H. Chen, G. Saraf, Y. Lu, A. Hagfeldt and G. Boschloo, *J. Phys. Chem. B*, 2006, **110**, 16159.
4 J. Lahiri and M. Batzill, *J. Phys. Chem. C*, 2008, **112**, 4304.

5 A. Van Dijken, E. Meulenkamp, D. Vanmaekelbergh and A. Meijerink, *J. Lumin.*, 2000, **87**, 454.
6 C. Zhang, K. Li, S. Song and D. Xue, *Chemistry*, 2013, **19**, 6329.
7 N. Hongsith, E. Wongrat, T. Kerdcharoen and S. Choopun, *Sens. Actuators, B*, 2010, **144**, 67.
8 C. Xu, J. Tamaki, N. Miura and N. Yamazoe, *Sens. Actuators, B*, 1991, **3**, 147.
9 C. Sun and D. Xue, *J. Phys. Chem. C*, 2013, **117**, 5505.
10 C. Sun and D. Xue, *Sci. Adv. Mater.*, 2013, **5**, 909.
11 C. Sun, S. Song, D. Xue and H. Zhang, *Funct. Mater. Lett.*, 2012, **05**, 1230002.
12 M. Chen, Z. Wang, D. Han, F. Gu and G. Guo, *J. Phys. Chem. C*, 2011, **115**, 12763.
13 P. Zhu, J. Zhang, Z. Wu and Z. Zhang, *Cryst. Growth Des.*, 2008, **8**, 3148.
14 Z. Wang, X. Qian, J. Yin and Z. Zhu, *Langmuir*, 2004, **20**, 3441.
15 X. W. Li, P. Sun, T. L. Yang, J. Zhao, Z. Y. Wang, W. N. Wang, Y. P. Liu, G. Y. Lu and Y. Du, *CrystEngComm*, 2013, **15**, 2949.
16 B. Liu and H. C. Zeng, *Chem. Mater.*, 2007, **19**, 5824.
17 J. Liu, H. Xia, D. Xue and L. Lu, *J. Am. Chem. Soc.*, 2009, **131**, 12086.
18 J. Liu, W. Liu, K. Chen, S. Ji, Y. Zhou, Y. Wan, D. Xue, P. Hodgson and Y. Li, *Chemistry*, 2013, **19**, 9811.
19 W. Liu, J. Liu, K. Chen, S. Ji, Y. Wan, Y. Zhou, D. Xue, P. Hodgson and Y. Li, *Chemistry*, 2014, **20**, 824.
20 J. Y. Lao, J. G. Wen and Z. F. Ren, *Nano Lett.*, 2002, **2**, 1287.
21 M. R. Alenezi, S. J. Henley, N. G. Emerson and S. R. P. Silva, *Nanoscale*, 2013, **6**, 235.
22 Y. Yang, D. S. Kim, R. Scholz, M. Knez, S. M. Lee, U. Gösele and M. Zacharias, *Chem. Mater.*, 2008, **20**, 3487.
23 F. Caruso, *Adv. Mater.*, 2011, **13**, 11.
24 J. Liu, S. Z. Qiao, S. Budi Hartono and G. Q. Lu, *Angew. Chem.*, 2010, **122**, 5101.
25 K. Kamata, Y. Lu and Y. Xia, *J. Am. Chem. Soc.*, 2003, **125**, 2384.
26 W. Zhang, H. Ming, J. Song, Y. G. Guo, S. F. Zheng, L. S. Zhong, W. G. Song and L. J. Wan, *Adv. Mater.*, 2008, **20**, 1160.
27 L. Wang, T. Fei, J. Deng, Z. Lou, R. Wang and T. Zhang, *J. Mater. Chem.*, 2012, **22**, 18111.
28 I. Lee, J. B. Joo, Y. Yin and F. Zaera, *Angew. Chem.*, 2011, **123**, 10390.
29 N. F. Hamedani, A. R. Mahjoub, A. A. Khodadadi and Y. Mortazavi, *Sens. Actuators, B*, 2011, **156**, 737.
30 K. Chen, S. Song and D. Xue, *CrystEngComm*, 2013, **15**, 10028.
31 J. Wu and D. Xue, *Nanosci. Nanotechnol. Lett.*, 2011, **3**, 371.
32 W. Shi, S. Song and H. Zhang, *Chem. Soc. Rev.*, 2013, **42**, 5714.
33 Y. Yin, R. M. Rioux, C. K. Erdonmez, S. Hughes, G. A. Somorjai and A. P. Alivisatos, *Science*, 2004, **304**, 711.
34 J. Liu, Y. Zhou, J. Wang, Y. Pan and D. Xue, *Chem. Commun.*, 2011, **47**, 10380.
35 I. Bilecka and M. Niederberger, *Nanoscale*, 2010, **2**, 1358.
36 M. Baghbanzadeh, L. Carbone, P. D. Cozzoli and C. O. Kappe, *Angew. Chem., Int. Ed.*, 2011, **50**, 11312.
37 J. J. Wu, H. I. Wen, C. H. Tseng and S. C. Liu, *Adv. Funct. Mater.*, 2004, **14**, 806.
38 H. Zhang, X. Ma, J. Xu, J. Niu and D. Yang, *Nanotechnology*, 2003, **14**, 423.
39 J. Liu, F. Liu, K. Gao, J. Wu and D. Xue, *J. Mater. Chem.*, 2009, **19**, 6073.
40 J. Liu, W. Liu, S. Ji, Y. Wan, M. Gu, H. Yin and Y. Zhou, *Chemistry*, 2014, **20**, 5815.
41 H. C. Zeng, *Curr. Nanosci.*, 2007, **3**, 177.
42 N. Yamazoe and K. Shimanoe, *Sens. Actuators, B*, 2009, **138**, 100.
43 N. Yamazoe and K. Shimanoe, *Sens. Actuators, B*, 2011, **154**, 277.
44 Z. Gergintschew, H. Förster, J. Kostiza and D. Schipanski, *Sens. Actuators, B*, 1995, **26**, 170.
45 J. C. Belmonte, J. Manzano, J. Arbiol, A. Cirera, J. Puigcorbé, A. Vilà, N. Sabaté, I. Gràcia, C. Cané and J. R. Morante, *Sens. Actuators, B*, 2006, **114**, 881.
46 N. J. Dayan, S. Sainkar, R. Karekar and R. Aiyer, *Thin Solid Films*, 1998, **325**, 254.
47 P. Sun, W. Zhao, Y. Cao, Y. Guan, Y. F. Sun and G. Y. Lu, *CrystEngComm*, 2011, **13**, 3718.